

Article

Not peer-reviewed version

Synthesis and Characterization of Iron Bispyridine Bisdicyanamide, $\text{Fe}[\text{C}_5\text{H}_5\text{N}]_2[\text{N}(\text{CN})_2]_2$

Laura Henrich , Peter C Müller , Jan Hempelmann , [Markus Mann](#) , Jan Van Leusen , [Simon Steinberg](#) ,
[Richard Dronskowski](#) *

Posted Date: 29 May 2023

doi: 10.20944/preprints202305.1978.v1

Keywords: crystal structure; iron; pyridine; dicyanamide; quantum chemistry; magnetism



Preprints.org is a free multidiscipline platform providing preprint service that is dedicated to making early versions of research outputs permanently available and citable. Preprints posted at Preprints.org appear in Web of Science, Crossref, Google Scholar, Scilit, Europe PMC.

Copyright: This is an open access article distributed under the Creative Commons Attribution License which permits unrestricted use, distribution, and reproduction in any medium, provided the original work is properly cited.

Article

Synthesis and Characterization of Iron Bispyridine Bisdicyanamide, $\text{Fe}[\text{C}_5\text{H}_5\text{N}]_2[\text{N}(\text{CN})_2]_2$

Laura Henrich ¹, Peter C. Müller ¹, Jan Hempelmann ¹, Markus Mann ^{1,2}, Jan van Leusen ¹, Simon Steinberg ¹ and Richard Dronskowski ^{1,3,*}

¹ Chair of Solid State and Quantum Chemistry, Institute of Inorganic Chemistry, RWTH Aachen University, 52056 Aachen, Germany. Fax: +49 241 80-92642; Tel: +49 241 80-93642

² Institute of Energy and Climate Research (IEK-1) Materials Synthesis and Processing, Forschungszentrum Jülich GmbH, Wilhelm-Johnen-Straße, 52425 Jülich, Germany

³ Hoffmann Institute of Advanced Materials, Shenzhen Polytechnic, 7098 Liuxian Blvd, Nanshan District, Shenzhen, China

* Correspondence: drons@HAL9000.ac.rwth-aachen.de

Abstract: $\text{Fe}[\text{C}_5\text{H}_5\text{N}]_2[\text{N}(\text{CN})_2]_2$ (**1**) was synthesized from a reaction of stoichiometric amounts of $\text{NaN}(\text{CN})_2$ and $\text{FeCl}_2 \cdot 4 \text{H}_2\text{O}$ in a methanol/pyridine solution. Single-crystal and powder diffraction show that **1** crystallizes in the monoclinic space group $I2/m$ (no. 12), different from $\text{Mn}[\text{C}_5\text{H}_5\text{N}]_2[\text{N}(\text{CN})_2]_2$ ($P2_1/c$, no. 14) due to tilted pyridine rings, with $a = 7.453(7) \text{ \AA}$, $b = 13.167(13) \text{ \AA}$, $c = 8.522(6) \text{ \AA}$, $\beta = 114.98(6)^\circ$ and $Z = 2$. ATR-IR, AAS, and CHN measurements confirm the presence of dicyanamide and pyridine. Thermogravimetric analysis shows that π -stacking interactions of the pyridine rings play an important role in structural stabilization. Based on DFT-optimized structures, a chemical bonding analysis was performed using a local-orbital framework by projection from a plane-wave basis. The resulting bond orders and atomic charges are in good agreement with the expectations based on the structure analysis. SQUID magnetic susceptibility measurements show a high-spin state Fe^{II} compound with predominantly antiferromagnetic exchange interactions at lower temperatures.

Keywords: crystal structure; iron; pyridine; dicyanamide; quantum chemistry; magnetism

1. Introduction

Solid-state materials containing pseudo elements such as cyanide [1–8], carbodiimide, and cyanamide [9–18] have gained a lot of interest over the last decades, in particular because those complex anions allow to mimic halide or chalcogenide chemistry with much more covalent nitrogen atoms. Another interesting pseudo-halide entity, the dicyanamide anion (dca), has gained less attention but fascinates by its structural behavior owing to its boomerang-shaped appearance. One of its outstanding properties is the ability to stabilize high-spin states due to the weaker ligand field in comparison to cyanide. In addition, the dicyanamide anion can coordinate up to four cations, due to the free electron pairs and the negative charge at the nitrogen atoms. Therefore, dca may act as a bridging ligand between metals [19–25].

3d metal dicyanamides can occur in the so called α - and β -structures. In the α -structure, all nitrogen atoms of the dca moiety are μ -1,3,5 bridging ligands, and the metal atom is octahedrally surrounded by nitrogen atoms of six dca units. This results in a rutile-like 3D network. In the β -structure, only the terminal nitrogen atoms are coordinated to the metal (μ -1,5 bridging), resulting in the metal adopting a tetrahedral coordination of four dca units, thereby forming a layered structure. Due to the boomerang shape of the dca units, the layers are zigzag shaped. The α -structure is known for 3d metals in oxidation states not in favor of Jahn-Teller distortion (e.g., Mn [26,27], Fe, Co, Ni [28]) [29]. Besides $\text{Cu}(\text{dca})$ [30], a β -structure is also known for $\text{Co}(\text{dca})_2$ [31] and $\text{Zn}(\text{dca})_2$ [32]. Due to the rutile-like network, 3d metal dicyanamides in the α -structure exhibit cooperative magnetism making them interesting research targets [27–29]. On the other hand, dicyanamides crystallizing in the β -

structure feature free accessibility to the metal as a consequence of their layered structure, a property of potential use in heterogeneous catalysis [23–32].

By introducing neutrally charged, non-bridging ligands *L* (e.g. DMF, EtOH, pyridine [33,34], pyridazine [35,36], ammonia [37,38]) to these 3*d* metal dicyanamides, both structure and properties change to a structure type *between* the α - and the β -structures. In the latter structure type, only the terminal nitrogen atoms of the dca units are μ -1,5 bridging the metals, as said before, so the additional *L* ligands complete the octahedral metal coordination. The dca units and metals form either 2*D* layers or 1*D* chains, analogous to the β -structure of pure 3*d* metal dicyanamide compounds. Due to the additional ligands, the different layers or chains can interact with each other leading, for example, to the formation of hydrogen bonds or π -stacking stabilizing the compound. These in-between structures mainly exhibit paramagnetic behavior instead of cooperative magnetism [33,34,37,38]. In this paper, we discuss the synthesis and characterization of a new $ML_2[N(CN)_2]_2$ compound: $Fe[C_5H_5N]_2[N(CN)_2]_2$.

2. Results and Discussion

2.1. Structural Description and Discussion

The crystal structure of $Fe[C_5H_5N]_2[N(CN)_2]_2$ was determined and confirmed based on several X-ray diffraction experiments at ambient temperature (300 K) as well as 100 K. Thorough inspections of these data pointed to the monoclinic system ($a = 7.453(7)$ Å, $b = 13.167(13)$ Å, $c = 8.522(6)$ Å, $\beta = 114.98(6)^\circ$), while the structure was solved and refined in space group $I2/m$ (no. 12). In this context, it should be noted that the previously reported $Mn[C_5H_5N]_2[N(CN)_2]_2$ crystallizes in the space group $P2_1/c$ (no. 14) [31]. Therefore, the powder as well as single-crystal X-ray diffraction data were carefully examined in order to confirm the choice of an *I*-centered monoclinic lattice for the iron-containing species (see below and *Materials and Methods* section for a full discussion regarding the structure determination).

Each unit cell comprises two formula units, while the bond lengths of the dca units in the iron-containing compound are consistent with data provided for such units in the literature [33,38]. In the dca unit, the distance of the outer C–N bond is $d(N2-C4) = 1.150(7)$ Å, while the length of the inner C–N bond is $d(C4-N3) = 1.308(6)$ Å. Such C–N distances are indicative of an inner single bond and an outer triple bond, in harmony with a simple Lewis sketch. The angles of the dca units are $\angle(N2-C4-N3) = 174.7(5)^\circ$ and $\angle(C4-N3-C4) = 119.5(6)^\circ$ which are also in good agreement with data in the literature [33,38]. The iron atoms are coordinated by four equatorially arranged dca units and additionally by the nitrogen atoms of two pyridine rings located in *trans* position (Figure 1, left). As a consequence, the coordinating nitrogen atoms form an almost ideal octahedron with distances of $d(Fe-N1)_{pyridine} = 2.192(11)$ Å and $d(Fe-N2)_{dca} = 2.166(5)$ Å in analogy to the manganese-containing compound reported in the literature ($d(Mn-N)_{pyridine} = 2.271(3)$ Å, $d(Mn-N)_{dca} = 2.226(3)$ Å). Unlike 3*d* metal dicyanamides, these compounds show μ -1,5 bridging in which the central nitrogen atom of the dca unit is not bonded to the metal. Indeed, the dicyanamides form bridging ligands, which connect the iron atoms within 1*D* chains. The pyridine rings of the different chains are intercalated with each other (Figure 1, right).

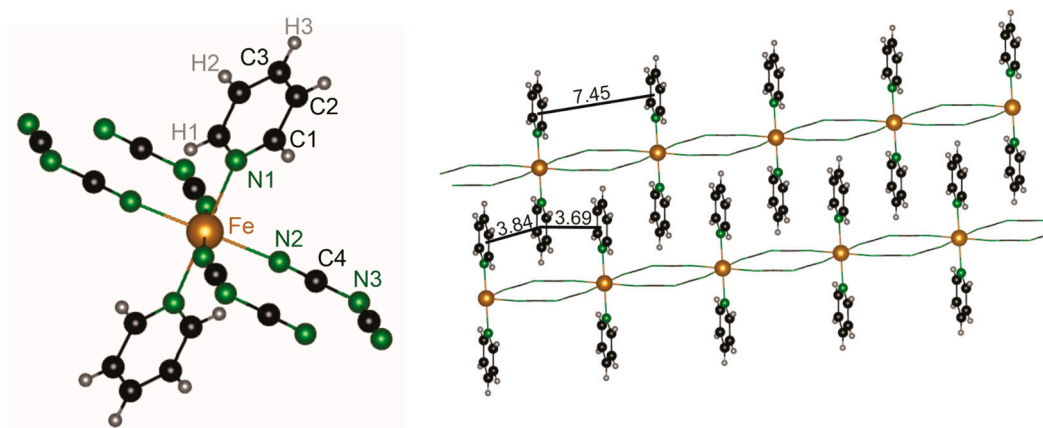


Figure 1. Coordination sphere of the iron atoms in $\text{Fe}[\text{C}_5\text{H}_5\text{N}]_2[\text{N}(\text{CN})_2]_2$ (left) and intercalation of pyridine rings within different chains (right). For clarity, the atoms of the dca units were removed in the right subfigure.

This results in the formation of 2D layers in which the pyridine rings play an important role in stabilizing the structure. A view along the *a*-axis reveals the almost perpendicular N–Fe–N angle of $\angle(\text{N}2\text{--Fe--N}2) = 91.6(3)^\circ$. Looking along the *b*-axis, another structural peculiarity becomes apparent. The pyridine rings of different 2D-layers are ordered in a parallel manner. Notably, the pyridine rings in the manganese-containing compound are tilted by circa 17° individually, alternating every second layer [33]. This circumstance explains the cancellation of translation symmetry and, therefore, the symmetry reduction of the manganese-containing compound in comparison to the iron-containing species. The distances between the intercalated rings alternate between 3.844(17) Å and 3.692(18) Å, which is well within the range of a typical π -stacking distance [39,40]. Seemingly, this stacking additionally stabilizes the substance that is neither sensitive to air nor moisture, even insoluble in water or selected organic solvents.

Because the anisotropic atomic displacement parameters (ADPs) corresponding to certain atoms of the pyridine rings are evidently elongated along the *c* direction, we also probed if the crystal structure of the iron-containing species could undergo a structural transition to that of the manganese-containing compound. Therefore, additional powder X-ray diffraction experiments and Rietveld refinements of the recorded data were carried out at different temperatures. The results of the refined lattice parameters at 300 K (Figure 2, Table S1) is in good agreement with those obtained in the single-crystal X-ray diffraction experiments ($R_B = 4.67\%$), while the 100 K measurement could not be refined due to the X-ray diffraction mode chosen (reflection, not transmission). Nonetheless, the reflection data show that all reflections could be described with the theoretical pattern generated by the single crystal measurement, the deficiencies showing up in the profiles. Further Rietveld refinements based on the structure model of the manganese-containing compound did not yield a reasonable model. We therefore conclude that the aforementioned structural transition is not evident for the iron-containing species between 300 and 100 K, possibly at even lower temperatures. Based on the single-crystal X-ray diffraction data, we checked if a modulated structure model might show up from a temperature-dependent rattling of the pyridine rings around the N1–C3–H3 axis; yet, there was also no clear evidence of a modulated structure model. Therefore, further research including high-quality neutron diffraction experiments within a broader temperature range might be needed to possibly monitor a movement of the pyridine rings.

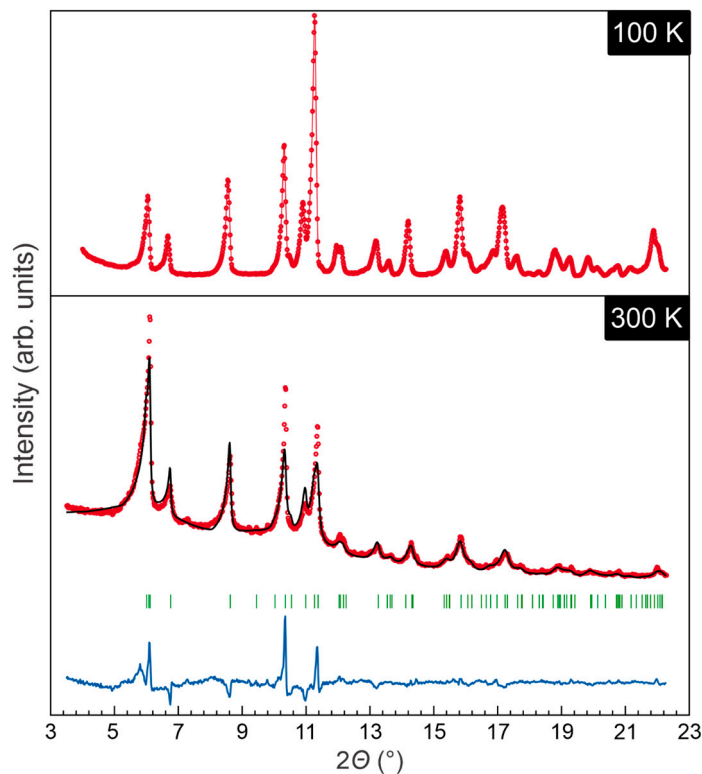


Figure 2. Comparison of the X-ray reflection-geometry measurement at 100 K (top) and the Rietveld refinement of the transition-geometry measurement at 300 K (bottom) with measured data in red, fitted pattern in black, Bragg positions in green, and difference curve in blue. .

2.2. Elemental Analysis

The atomic absorption spectroscopy (AAS) and CHN measurement show the presence of iron, carbon, nitrogen, and hydrogen (Table 1). The value for iron is slightly larger, and those of carbon, hydrogen, and nitrogen slightly smaller than expected. A plausible explanation might be given by the presence of other ions bound in the sample, causing the carbon, hydrogen, and nitrogen values to decrease. For example, the surface of the compound could still be contaminated by chloride ions or water molecules. Since the compound is a microcrystalline powder, the surface is relatively large and could therefore influence the overall composition.

Table 1. Theoretical and experimental data for Fe[C₅H₅N]₂[N(CN)₂]₂ of the AAS (iron) and CHN (carbon, hydrogen, nitrogen) measurement.

Element	Fe	C	H	N
Theoretical (%)	16.13	48.58	2.91	32.37
Experimental (%)	17.3(2)	45.9(1)	2.60(8)	31.4(2)
Deviation (abs.)	+ 1.17	− 2.73	− 0.30	− 1.02

2.3. Attenuated Total Reflection Infrared Spectroscopy (ATR-IR)

The obtained IR frequencies show the presence of both the dca unit and the pyridine ring (Figure S1), in good agreement with the literature [21,36]. For a better comparison, the theoretical vibrations of Fe[C₅H₅N]₂[N(CN)₂]₂, Fe[N(CN)₂]₂ and pyridine were distinguished with DFT and show a good fit with the experimental data. The assignments of the vibrations can be found in Table S5.

2.4. Thermogravimetric Analysis (TGA)

The TGA data are depicted as a mass fraction vs. temperature plot in Figure 3.

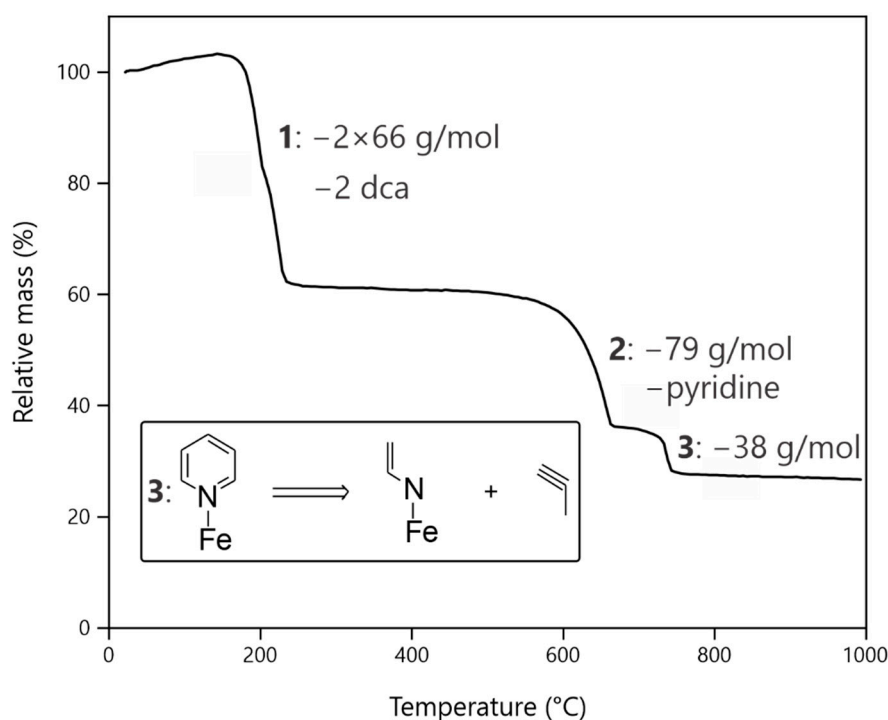


Figure 3. Thermogravimetric analysis of $\text{Fe}[\text{C}_5\text{H}_5\text{N}]_2[\text{N}(\text{CN})_2]_2$ measured in nitrogen flow; inset: possible decomposing reaction in step 3.

Mass losses occur three times at approx. 180 (1), 620 (2), and 670 °C (3). Assuming that the substance is the desired compound ($\text{Fe}[\text{C}_5\text{H}_5\text{N}]_2[\text{N}(\text{CN})_2]_2$), the first mass loss (1) of 100 to 61 % fits the cleavage of two dca units (132.08 g/mol), leaving $\text{Fe}[\text{C}_5\text{H}_5\text{N}]_2$ behind. The mass loss at 620 °C (2) can be explained by the cleavage of one pyridine ring per iron atom (79.10 g/mol). The mass loss is somewhat surprising at such a high temperature, since the boiling point of pyridine is at 115 °C under standard conditions. So, significant covalency in the bond between iron and pyridine does exist, but also π -stacking between pyridine rings. According to the literature, the cleavage temperature of pyridine is about 400 °C [41], which is almost 200 °C below the temperature needed for splitting a pyridine ring from the compound. The last decomposition step at 670 °C (3) fits a mass loss of 38.06 g/mol and can therefore not be explained by the cleavage of another pyridine ring. Comparison with the literature indicates that pyridine may decompose into many different components although there is no decomposition fitting a mass loss of about 38 g/mol, while leaving a reasonable iron residue [42,43]. The high temperature may have caused the ring to split, resulting in the cleavage of a C_3H_3 fragment (Figure 3, inset). These fragments could have reacted with each other after cleavage to saturate the free-binding sites on the carbon. Such a reaction was not tracked in the TGA but seems the most reasonable to us.

In summary, TGA confirms the presence of the proposed fragments in the compound. Furthermore, the interactions of the pyridine rings have a very large influence on the stability of the compound, which is already reflected in its low solubility.

2.5. Chemical Bonding Analysis

To examine the chemical bonding situation in $\text{Fe}[\text{C}_5\text{H}_5\text{N}]_2[\text{N}(\text{CN})_2]_2$, the crystal orbital bond index (COBI) [44] as well as Löwdin charges [45] were calculated using LOBSTER. In contrast to common bonding indicators for solids, COBI's interpretation is almost trivial as its energy integral, the ICOBI, directly translates into the covalent bond order between any two atoms. ICOBI as well as the charges for all respective atoms are shown in Figure 4.

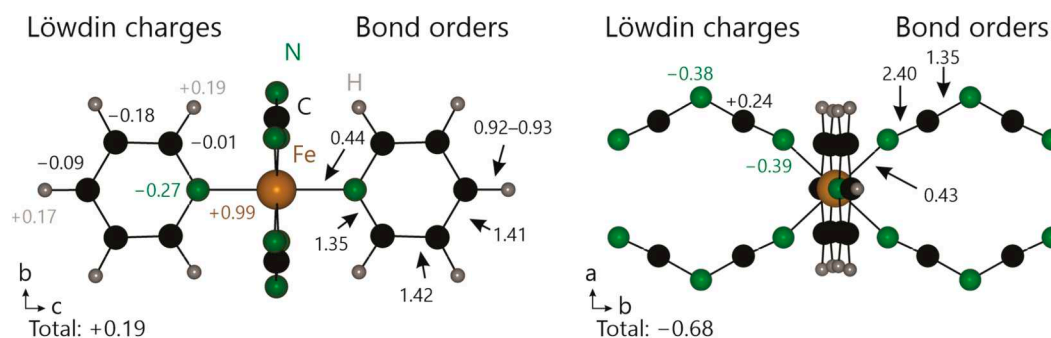


Figure 4. ICOBIs and Löwdin charges of $\text{Fe}[\text{C}_5\text{H}_5\text{N}]_2[\text{N}(\text{CN})_2]_2$; left: in a direction, right: in c direction.

All calculated bonding descriptors are in good agreement with expectations from a simple Lewis picture: both C–C and C–N bonds in the pyridine rings have an ICOBI of about 1.4, indicative of the aromatic ring. The C–H bonds are single bonds, as expressed by ICOBI ≈ 0.92 . With an overall charge of +0.19, pyridine may be considered almost neutral. The dicyanamide unit shows a bond order of 2.4 between nitrile nitrogen and carbon, while the bond order between amide nitrogen and carbon is 1.35. In combination, both bond orders indicate the presence of mesomerism between the $\text{N}\equiv\text{C}-\text{N}$ and $\text{N}=\text{C}=\text{N}$ forms of the dicyanamide molecule. The calculated bond orders in the dca unit match those in the proposed structure of $\text{Fe}[\text{C}_5\text{H}_5\text{N}]_2[\text{N}(\text{CN})_2]_2$. The charge on the formally divalent iron atom indirectly suggests a strong covalent moiety in the coordinative bonds between iron and nitrogen, confirmed by the ICOBIs of 0.43–0.44 for the Fe–N bonds.

2.6. Magnetic Properties

The magnetic data of $\text{Fe}[\text{C}_5\text{H}_5\text{N}]_2[\text{N}(\text{CN})_2]_2$ normalized to a single Fe^{II} center are displayed in Figure 5 as $\chi_m T$ vs. T plot at 0.1 T and as M_m vs. B plot at 2.0 K (inset).

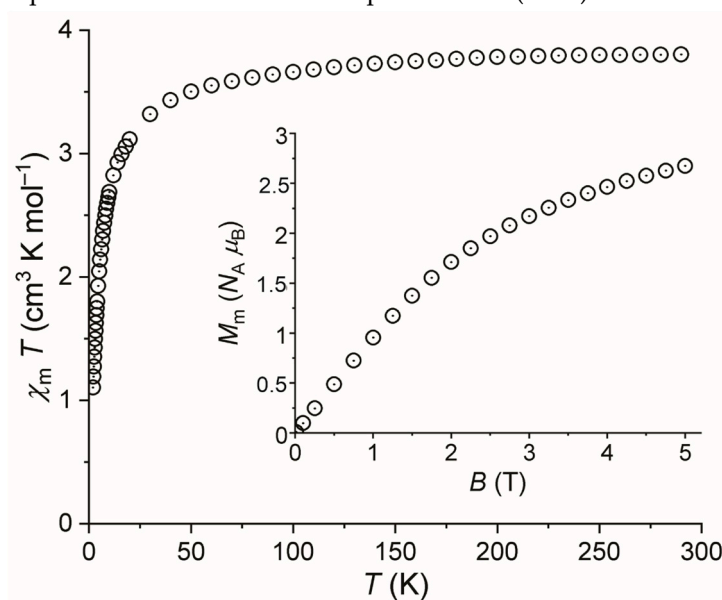


Figure 5. Temperature dependence of $\chi_m T$ of $\text{Fe}[\text{C}_5\text{H}_5\text{N}]_2[\text{N}(\text{CN})_2]_2$ at 0.1 T; inset: molar magnetization M_m vs. applied magnetic field B at 2.0 K.

At 290 K, $\chi_m T$ is $3.80 \text{ cm}^3 \text{K mol}^{-1}$, which is within the expected [46] range of $3.2\text{--}4.1 \text{ cm}^3 \text{K mol}^{-1}$ of an isolated high spin Fe^{II} center. This range is above the spin-only value of $3.00 \text{ cm}^3 \text{K mol}^{-1}$ (for $S = 2$), since orbital contributions are not fully quenched for an octahedrally coordinated $3d^6$ ion. Upon cooling the compound, the values of $\chi_m T$ continuously decrease and drop off at temperatures below 50 K reaching $1.11 \text{ cm}^3 \text{K mol}^{-1}$ at 2 K. At this temperature, the molar magnetization is an almost linear

function of the applied magnetic field up to about 1.5 T. Upon increasing fields, M_m increases at decreasing rate without reaching saturation at the highest fields of the experimental set-up of 5.0 T. The value of M_m is $2.7 N_A \mu_B$ which is well below the saturation value of about $4.5 N_A \mu_B$ estimated from the value of $\chi_m T$ at 290 K. The significant decrease of $\chi_m T$ at temperatures below 100 K is partly due to the thermal depopulation of the energy states of the Fe^{II} center split by electron-electron inter-repulsion, ligand field, and spin-orbit coupling. However, the main contribution is due to predominantly antiferromagnetic, yet weak exchange interaction between neighboring Fe^{II} centers. This is also evident from the M_m vs. B curve, because the magnetization of an isolated high spin Fe^{II} center with distorted octahedral symmetry is not expected to reach saturation at 5 T and 2 K due to the ground state being characterized by distinct mixing of energy states with different magnetic moments. Besides the latter, such Fe^{II} centers are additionally characterized by magnetic anisotropy that yields lower values of M_m since they represent the mean values obtained from a sample of randomly oriented crystallites, i.e., a powderous material. However, both effects result in a value of M_m of about $1 N_A \mu_B$ below the saturation value and a slightly smaller slope at 5 T and 2 K than shown in Figure 5. Therefore, the even lower value of M_m at this temperature and field also reveals weak, predominantly antiferromagnetic exchange interactions within the compound.

3. Materials and Methods

3.1. Synthesis

$\text{Fe}[\text{C}_5\text{H}_5\text{N}]_2[\text{N}(\text{CN})_2]_2$ was synthesized by adding $\text{FeCl}_2 \cdot 4 \text{H}_2\text{O}$ (0.9942 g, 5 mmol) to a stirring solution of $\text{NaN}(\text{CN})_2$ (0.8904 g, 10 mmol, 2 Eq.) in 100 mL methanol. Afterwards, pyridine (1.5 mL, ≈ 18.5 mmol, 2.9 Eq.) was added dropwise. The beige-colored product precipitated immediately, was filtered, dried, and appeared as a crystalline powder containing a few single crystals, which were stable against air and moisture.

3.2. Single Crystal Diffraction

The samples were selected from the bulk and placed at the top of glass fibers with the aid of grease. The sets of single-crystal X-ray intensity data were collected at 100 K on a Bruker® APEX CCD diffractometer (Bruker Inc., Madison, WI; Mo- $\text{K}\alpha_1$ radiation, $\lambda = 0.71073 \text{ \AA}$) that was equipped with an Oxford® Cryostream 700 to control the temperature of the measurements. Initial indexing of the collected data pointed to a C-centered monoclinic lattice setting that was used for subsequent processing of the data. The raw intensity data were integrated by using the program SAINT [47], while an absorption correction was accomplished utilizing the SADABS code [48]. Applications of the reflection conditions to the data sets were accomplished by means of the XPREP algorithms within the APEX II suite [49] and pointed to the space group $I2/m$, which was also used for the final structure solutions and refinements. The crystal structure was solved using direct methods (SHELXS-97) and refined in full-matrix least squares on F^2 (SHELXL-2014) which also included anisotropic atomic displacement parameters [50,51,]. In the framework of the data analysis and structure solution, we became aware of reflections of very weak intensities which translated into the large R_i value for all data, while somewhat enlarged anisotropic atomic displacement parameters were evident for certain sites assigned to the pyridine rings. Therefore, extensive examinations were undertaken to check for the presence of a space group being different from $I2/m$ or for the occurrence of a modulated structure as a consequence of possible elongations of the pyridine rings; yet, none of our attempts could satisfactorily reveal the existence of one of the aforementioned phenomena, while close inspections of the intensity data sets did not indicate the presence of any sort of twinning. In addition, we probed if positional disorder could be present for the pyridine rings; yet, there were no hints pointing to such a scenario. Furthermore, we took into consideration to carry out a numerical absorption correction; yet, the size of the selected single crystal ($\leq 0.1 \text{ mm}$) hindered to conduct a numerical absorption correction so that a semi-empirical method had to be used in full line with the recommendations of the International Union of Crystallography. [52]

3.3. Powder X-Ray Diffraction

The powder sample was first loaded into a sample holder and then transferred to a Stoe® STADI MP diffractometer (Stoe & Cie, Darmstadt, Germany; Mo-K α_1 radiation, ($\lambda = 0.71073 \text{ \AA}$), which was used to collect the powder X-ray diffraction data set in transmission mode at 300 K, while the 100 K measurement was performed in reflection mode under vacuum. The measurements were controlled with the WinXPow® program [53], which was also used for further processing of the raw data, while the Rietveld refinements of the collected powder X-ray diffraction patterns for the measurement at $T = 300 \text{ K}$ were performed with *FullProf Suite* [54] and a formally pseudo-Voigt profile function of full Lorentzian shape to profit from the better asymmetry correction. The atomic positions and ADPs were taken from the single crystal refinement and were not refined. The results of this Rietveld refinement further confirmed the structural model determined on the basis of the single crystal X-ray diffraction experiments (see above).

3.4. Magnetic Measurements

A polycrystalline sample of $\text{Fe}[\text{C}_5\text{H}_5\text{N}]_2[\text{N}(\text{CN})_2]_2$ was compacted and immobilized into a cylindrical PTFE capsule. A Quantum Design® MPMS-5XL SQUID magnetometer (Quantum Design, San Diego, CA, USA) was employed to collect the magnetic data, which were acquired as a function of temperature (2–290 K at 0.1 T) and magnetic field (0.1–5 T at 2 K). The data were corrected for the diamagnetic contributions of the sample holder and the compound ($\chi_{\text{m,dia}} = -1.73 \cdot 10^{-4} \text{ cm}^3 \text{ mol}^{-1}$).

3.5. Infrared Spectroscopy (ATR-IR)

Fine powders of $\text{Fe}[\text{C}_5\text{H}_5\text{N}]_2[\text{N}(\text{CN})_2]_2$ were loaded in a sample holder, while the IR spectra (absorbance versus wavelength) were collected on a Bruker® alpha II spectrometer (Bruker, Madison, WI, USA). The program OPUS was used for the control of the measurements as well as processing of the raw data.

3.6. Thermogravimetric Analysis (TGA)

Thermogravimetric analyses were performed using a Netzsch® STA 409 C (Netzsch, Selb, Germany). The compound was heated and weighed in nitrogen flow in the temperature range from 25 to 1000 °C with a heating rate of 5 °C/min.

3.7. Atomic Absorption Spectroscopy (AAS)

For the determination of the iron content, approx. 50 mg of each sample were dissolved three times in 5 mL concentrated HCl and quantitatively transferred to a 100 mL volumetric flask. To each sample, 10 mL of a 0.1 % KCl solution was added as an ionization buffer, and the volumetric flasks were filled up to the calibration mark. The sample solutions were analyzed using a novAA300 AAS from Analytik Jena, Germany, the reference solutions were prepared from a certified iron standard (1000 mg/L) from Kraft. A six-element multi-HKL from L.O.T. Oriel served as the emission source.

3.8. Computational Details

All structures were optimized via density functional theory (DFT) using the *Vienna Ab initio Simulation Package* (VASP) [55–58]. The electronic wave functions were modeled with PAW pseudopotentials [59] with a kinetic energy plane-wave cutoff of 500 eV. The exchange-correlation interactions were modeled using the generalized gradient approximation (GGA) as parametrized by Perdew, Burke and Ernzerhof and optimized for solids (PBEsol) [60] with an additional D3-correction term introduced by Grimme with Becke–Johnson damping [61,62]. The Brillouin-zone integration was done using Blöchl's tetrahedron method, employing \mathbf{k} -point meshes with densities between 0.02 and 0.04 \AA^{-3} [63]. Convergence of the calculations was assumed for energy differences of 10^{-4} eV for ionic steps and 10^{-6} eV for electronic steps.

After the structural optimization, a chemical bonding analysis was performed. Because the bonding analysis required the use of local orbitals whose nature is in stark contrast to that of the plane waves, the electronic ground-state wave functions were unitarily transformed onto a local-orbital basis using the *Local Orbital Basis Suite Towards Electronic-Structure Reconstruction* (LOBSTER) package [64–66]. The simulation of the lattice vibration was performed with the program *Phonopy* [67] according to the Hellmann–Feynman forces from VASP. A simulation of IR spectra was conducted based on phononic calculations and Born effective charges received using the methods described above and processed using the *JaGeo/IR* software package [68–71].

4. Conclusions

Herein, we report on the synthesis and characterization of iron bispyridine bisdicyanamide, $\text{Fe}[\text{C}_5\text{H}_5\text{N}]_2[\text{N}(\text{CN})_2]_2$, that is a new transition metal-containing compound with dca and pyridine ligands. The crystal structure was determined using single crystal as well as powder X-ray diffraction with particular regard to a possible motion of the pyridine rings; yet, a structural transition related to a reorientation of the pyridine rings could not be encountered based on X-ray diffraction. AAS, CHN, ATR-IR, and TGA measurements were performed to prove the composition. Additionally, the TGA indicates the high impact of the π -stacking regarding the structural stability. The bonding situation in the compound, examined with ICOBI and Löwdin charge analyses, agrees with the expectations based on structural analysis. Magnetic measurements evidence that $\text{Fe}[\text{C}_5\text{H}_5\text{N}]_2[\text{N}(\text{CN})_2]_2$ is a paramagnetic compound comprising high spin Fe^{II} centers. There are weak, predominantly antiferromagnetic exchange interactions between these atoms, observable at low temperatures. Considering structural information, these interactions are most likely of 1D nature between the Fe^{II} centers coupled through the dca ligands, i.e., along the $\text{Fe}-(\text{dca})_2\text{-Fe}$ -chains within the compound.

Supplementary Materials: Single-crystal data in CIF format can be downloaded as supporting information at: Preprints.org.

Author Contributions: Conceptualization – L.H.; Funding acquisition – R.D.; Investigation – L.H., P.M., J.H., J.v.L., M.M.; Methodology – L.H., P.M., S.S.; Project administration – L.H., R.D.; Resources – R.D.; Supervision – R.D.; Validation – S.S., R.D.; Visualization – L.H., P.M., J.v.L.; Writing – original draft – L.H.; Writing – review & editing – L.H., M.M., P.M., J.H., J.v.L., S.S., R.D.

Funding: Calculation time was provided by the Jülich Aachen Research Alliance (project no. jara0033).

Data Availability Statement: CCDC 2265156 contain the crystallographic data for this paper. These data can be obtained free of charge via <http://www.ccdc.cam.ac.uk/conts/retrieving.html> or from the CCDC, 12 Union Road, Cambridge CB21EZ; Fax: +44-1223-336033; E-Mail: deposit.ccdc.cam.ac.uk. All other data may be obtained from the corresponding author on reasonable request.

Acknowledgments: We would like to thank Kathrin Schmidt from the Welding and Joining Institute, RWTH Aachen University, for the AAS measurement and Noah Avraham from the Institute of Technical Chemistry, RWTH Aachen University, for the TGA measurements. Furthermore, we wish to thank Tobias Storp for the collections of the sets of single-crystal as well as powder X-ray diffraction data. Also, we thank Dr. Michal Fecik, Linda Reitz and Manuel Henrich for critical reading.

Conflicts of Interest: The authors declare no conflict of interest.

Sample Availability: Samples of the compound **1** are available from the authors.

References

1. Aigner, K.; Lengauer, W.; Rafaja, D.; Ettmayer, P.; *J. Alloys Compds.* **1994**, *215*, 121–126.
2. Bijvoet, J. M.; Lely, J. A.; *Recl. Trav. Chim. Pays-Bas* **1940**, *59*, 908–912.
3. Kareis, C. M.; Lapidus, S. H.; Stephens, P. W.; Miller, J. S.; *Inorg. Chem.* **2012**, *51*, 3046–3050.
4. Lely, J. A.; Bijvoet, J. M.; *Recl. Trav. Chim. Pays-Bas* **1942**, *61*, 244–252.
5. Williams, D. J.; Partin, D. E.; Lincoln, F. J.; Kouvetakis, J.; O'Keeffe, M.; *J. Solid State Chem.* **1997**, *134*, 164–169.
6. Williams, D. J.; Kouvetakis, J.; O'Keeffe, M.; *Inorg. Chem.* **1998**, *37*, 4617–4620.
7. Rowe, J. M.; Rush, J. J.; Lüty, F.; *Phys. Rev. B: Condens. Matter Mater. Phys.* **1984**, *29*, 2168–2170.

8. Williams, D. J.; Pleune, B.; Leinenweber, K.; Kouvetakis, J.; *J. Solid State Chem.* **2001**, *159*, 244–250.
9. Arayamparambil, J. J.; Mann, M.; Liu, X.; Alfredsson, M.; Dronskowski, R.; Stievano, L.; Sougrati M. T.; *ACS Omega* **2019**, *4*, 4339–4347.
10. Berger, U.; Schnick, W.; *J. Alloys Compds.* **1994**, *206*, 179–184.
11. Down, M. G.; Haley, M. J.; Hubberstey, P.; Pulham, R. J.; Thunder, A.E.; *J. Chem. Soc., Dalton Trans.* **1978**, 1407.
12. Dronskowski, R.; *Z. Naturforsch. B* **1995**, *50*, 1245–1251.
13. Jürgens, B.; Irran, E.; Schneider, J.; Schnick, W.; *Inorg. Chem.* **2000**, *39*, 665–670.
14. Liu, X.; Dronskowski, R.; Kremer, R. K.; Ahrens, M.; Lee, C.; Whangbo, M.; *J. Phys. Chem. C* **2008**, *112*, 11013–11017.
15. Krott, M.; Liu, X.; Fokwa, P. T. B.; Speldrich, M.; Lueken, H.; Dronskowski, R.; *Inorg. Chem.* **2007**, *46*, 2204–2207.
16. Liu, X.; Krott, M.; Müller, P.; Hu, C.; Lueken, H.; Dronskowski, R.; *Chem. Eur. J.* **2005**, *44*, 3001–3003.
17. Liu, X.; Stork, L.; Speldrich, M.; Lueken, H.; Dronskowski, R.; *Chem. Eur. J.* **2009**, *15*, 1558–1561.
18. Tang, X.; Xiang, H.; Liu, X.; Speldrich, M.; Dronskowski, R.; *Angew. Chem. Int. Ed.* **2010**, *49*, 4738–4742.
19. Reckeweg, O.; Wakabayashi, R. H.; DiSalvo, F. J.; Schulz, A.; Schneck, C.; Schleid, T.; *Z. Naturforsch. B* **2015**, *70*, 365–372.
20. Reckeweg, O.; DiSalvo, J. F.; Schulz, A.; Blaschowski, B.; Jagiella, S.; Schleid, T.; *Z. Anorg. Allg. Chem.* **2014**, *640*, 851–855.
21. Jürgens, B.; Irran, E.; Schnick, W.; *J. Solid State Chem.* **2001**, *157*, 241–249.
22. Kuhn, R. M.; *Chem. Ber.* **1961**, *94*, 3010–3015.
23. Britton, D.; Chow, Y. M.; *Acta Crystallogr., Sect. B: Struct. Sci. Cryst. Eng. Mater.* **1977**, *33*, 697–699.
24. Mann, M.; Reckeweg, O.; Nöthling, N.; Goddard, R.; Dronskowski, R.; *Inorganics* **2018**, *6*, 135–1–9.
25. Mann, M.; Reckeweg, O.; Dronskowski, R.; *Inorganics* **2018**, *6*, 108–1–7.
26. Kmety, C. R.; Huang, Q.; Lynn, J. W.; Erwin, R. W.; Manson, J. L.; McCall, S.; Crow, J. E.; Stevenson, K. L.; Miller, J. S.; Epstein, A. J.; *Phys. Rev. B Condens. Matter Mater. Phys.* **2000**, *62*, 5576–5588.
27. Manson, J. L.; Kmety, C. R.; Epstein, A. J.; Miller, J. S.; *Inorg. Chem.* **1999**, *38*, 2552–2553.
28. Manson, J. L.; Kmety, C. R.; Huang, Q.; Lynn, J. W.; Bendele, G. M.; Pagola, S.; Stephens, P. W.; Liable-Sands, L. M.; Rheingold, A. L.; Epstein, A. J.; Miller, J. S.; *Chem. Mater.* **1998**, *10*, 2552–2560.
29. Lappas, A.; Wills, A. S.; Green, M. A.; Prassides, K.; Kurmoo, M.; *Phys. Rev. B: Condens. Matter Mater. Phys.* **2003**, *67*, 144406.
30. Reckeweg, O.; Dinnebier, R. E.; Schulz, A.; Blaschkowski, B.; Schneck, C.; Schleid, T.; *Z. Naturforsch. B* **2017**, *72*, 159–165.
31. Jensen, P.; Batten, S. R.; Fallon, G. D.; Moubaraki, B.; Murray, K. S.; Price, D. J.; *Chem. Commun.* **1999**, 177–178.
32. Manson, J. L.; Lee, D. W.; Rheingold, A. L.; Miller, J. S.; *Inorg. Chem.* **1998**, *37*, 5966–5967.
33. Batten, S. R.; Jensen, P.; Kepert, C. J.; Kurmoo, M.; Moubaraki, B.; Murray, K. S.; Price, D. J.; *J. Chem. Soc., Dalton Trans.* **1999**, 2987–2997.
34. Huang, W.; Zhang, J.; Zhang, C.; *Acta Crystallogr., Sect. E* **2013**, *69*, m90.
35. Wöhlert, S.; Wriedt, M.; Jess, I.; Näther, C.; *Acta Crystallogr., Sect. E* **2012**, *68*, m965.
36. Wriedt, M.; *Dalton Trans.* **2011**, *40*, 886–898.
37. Reckeweg, O.; Schulz, A.; DiSalvo, F. J.; *Z. Naturforsch. B* **2013**, *68*, 296–300.
38. Mann, M.; Mroz, D.; Henrich, L.; Houben, A.; van Leusen, J.; Dronskowski, R.; *Inorg. Chem.* **2019**, *58*, 7803–7811.
39. Janiak, C.; *J. Chem. Soc., Dalton Trans.* **2000**, 3885–3896.
40. Kertesz, M.; *Chem.* **2019**, *25*, 400–416.
41. Chen, S.; Zhuo, H.; Chen, S.; Ge, Z.; Yuan, H.; Luo, J.; *Thermochimica Acta* **2012**, *543*, 281–287.
42. Sato, Y.; Matsunaga, T.; Takehiro, K.; Koyama, S.; Suzuki, T.; Ozawa, M.; *Energy Procedia* **2015**, *71*, 112–122.
43. Hore, N. R.; Russell, S. K.; *J. Chem. Soc., Perkin Trans.* **1998**, *2*, 269–276.
44. Müller, P. C.; Ertural, C.; Hempelmann, J.; Dronskowski, R.; *J. Phys. Chem. C* **2021**, *125*, 7959–7970.
45. Ertural, C.; Steinberg, S.; Dronskowski, R.; *RSC Adv.* **2019**, *9*, 29821–29830.
46. Elschenbroich, C.; Hensel, F.; Hopf, H.; Lueken, H.; *Magnetochemie*, Vieweg+Teubner, Wiesbaden, Germany, **1999**, 40.
47. SAINT+, version 7.68; Bruker AXS Inc., Madison, WI, USA, **2009**.
48. SADABS, version 2004/1; Bruker AXS Inc., Madison, WI, USA, **2009**.
49. APEX2 v2014.11-0, Bruker Nonius, Bruker AXS Inc.: Madison, WI, USA, **2003**, **2004**, **2005–2014**.
50. Sheldrick, G. M.; *Acta Crystallogr., Sect. A: Found. Crystallogr.* **2008**, *64*, 112–122.
51. Sheldrick, G. M.; *Acta Crystallogr., Sect. C: Struct. Chem.* **2015**, *71*, 3–8.
52. W. Massa, Kristallstrukturbestimmung, Vieweg+Teubner, Wiesbaden, Germany, **2009**.
53. WinXPow, version 2.23; STOE & Cie GmbH: Darmstadt, Germany, **2005**.
54. Rodríguez-Carvajal, *Phys. B: Condens. Matter* **1993**, *192*, 55–69.

55. Kresse, G., Furthmüller, J.; *Phys. Rev. B: Condens. Matter Mater. Phys.* **1996**, *54*, 11169–11186.
56. Kresse, G.; Hafner, J.; *Phys. Rev. B: Condens. Matter Mater. Phys.* **1993**, *47*, 558–561.
57. Kresse, G., Furthmüller, J.; *Comp. Mater. Sci.* **1996**, *6*, 15–50.
58. Kresse, G.; Joubert, D.; *Phys. Rev. B: Condens. Matter Mater. Phys.* **1999**, *59*, 1758–1775.
59. Blöchl, P. E.; *Phys. Rev. B: Condens. Matter Mater. Phys.* **1994**, *50*, 17953–17979.
60. Csonka, G. I.; Perdew, J. P.; Ruzsinszky, A.; Philipsen, P. H. T.; Lebegue, S.; Paier, J.; Vydrov, O. A.; Ángyán, J. G.; *Phys. Rev. B: Condens. Matter Mater. Phys.* **2009**, *79*, 155107.
61. Grimme, S.; Antony, J.; Ehrlich, S.; Krieg, H.; *J. Chem. Phys.* **2010**, *132*, 154104.
62. Grimme, S.; Ehrlich, S.; Goerigk, L.; *J. Comput. Chem.* **2011**, *32*, 1456–1465.
63. Monkhorst, H.J.; Pack, J. D.; *Phys. Rev. B* **1976**, *13*, 5188.
64. Maintz, S.; Deringer, V. L.; Tchougréeff, A. L.; Dronskowski, R.; *J. Comput. Chem.* **2016**, *37*, 1030–1035.
65. Maintz, S.; Deringer, V. L.; Tchougréeff, A. L.; Dronskowski, R.; *J. Comput. Chem.* **2013**, *34*, 2557–2567.
66. Nelson, R.; Ertural, C.; George, J.; Deringer, V. L.; Hautier, G.; Dronskowski, R.; *J. Comput. Chem.* **2020**, *41*, 1931–1940.
67. Togo, A.; *Scr. Mater.* **2015**, *108*, 1–5.
68. Giannozzi, P.; *J. Chem. Phys.* **1994**, *100*, 8537–8539.
69. Görne, A.; George, J.; van Leusen, J.; Dronskowski, R.; *Inorganics* **2017**, *5*, 10.
70. Zenodo. Available online: <https://zenodo.org/record/3241592#.Y9pBPq2ZO70> (accessed on 01.02.2023).
71. Karhánek, D.; Bučko, T.; Jürgen, J.; *J. Phys. Condens. Matter* **2010**, *22*, 265006.

Disclaimer/Publisher's Note: The statements, opinions and data contained in all publications are solely those of the individual author(s) and contributor(s) and not of MDPI and/or the editor(s). MDPI and/or the editor(s) disclaim responsibility for any injury to people or property resulting from any ideas, methods, instructions or products referred to in the content.